Quasiparticle and excitonic effects in the optical response of KNbO₃

Falko Schmidt,[*] Arthur Riefer, Wolf Gero Schmidt, and Arno Schindlmayr
Department Physik, Universität Paderborn, 33095 Paderborn, Germany

Mirco Imlau
School of Physics, Universität Osnabrück, Barbarastraße 7, 49076 Osnabrück, Germany

Florian Dobener, Nils Mengel, and Sangam Chatterjee
I. Physikalisches Institut and Center for Materials Research, Justus-Liebig-Universität Gießen, 35392 Gießen, Germany

Simone Sanna
Institut für Theoretische Physik and Center for Materials Research, Justus-Liebig-Universität Gießen, 35392 Gießen, Germany

The cubic, tetragonal, and orthorhombic phase of potassium niobate (KNbO₃) are studied based on density-functional theory. Starting from the relaxed atomic geometries, we analyze the influence of self-energy corrections on the electronic band structure within the *GW* approximation. We find that quasiparticle shifts widen the direct (indirect) band gap by 1.21 (1.44), 1.58 (1.55), and 1.67 (1.64) eV for the cubic, tetragonal, and orthorhombic phase, respectively. By solving the Bethe-Salpeter equation, we obtain the linear dielectric function with excitonic and local-field effects, which turn out to be essential for good agreement with experimental data. From our results, we extract an exciton binding energy of 0.6, 0.5, and 0.5 eV for the cubic, tetragonal, and orthorhombic phase, respectively. Furthermore, we investigate the nonlinear second-harmonic generation (SHG) both theoretically and experimentally. The frequency-dependent second-order polarization tensor of orthorhombic KNbO₃ is measured for incoming photon energies between 1.2 and 1.6 eV. In addition, calculations within the independent-(quasi)particle approximation are performed for the tetragonal and orthorhombic phase. The novel experimental data are in excellent agreement with the quasiparticle calculations and resolve persistent discrepancies between earlier experimental measurements and *ab initio* results reported in the literature.

I. INTRODUCTION

Potassium niobate (KNbO₃) [1] exhibits ferroelectric properties as well as strong optical nonlinearities and is therefore of high interest for technological applications, such as second-harmonic generation [2], piezoelectricity [3], and data storage [4]. Like many other perovskite materials, it also undergoes a sequence of structural phase transitions in different temperature regimes. Potassium niobate crystallizes at about 1325 K in a cubic structure (space group $Pm\bar{3}m$) and shows a transition to a tetragonal phase (space group $P4mm$) at 691 K, to an orthorhombic phase (space group $Bmm2$) at 498 K, and to a rhombohedral phase (space group $R3m$) at 263 K [5]. Furthermore, a monoclinic structure (space group Pm) was recently observed in nanomaterials [6].

While experimental studies are usually limited to the orthorhombic room-temperature phase [7–11], theoretical studies tend to concentrate on the cubic and tetragonal phase, whose simpler structure and higher degree of symmetry make them more amenable to computationally expensive first-principles simulations [12–15]. Although it is often claimed that these high-temperature phases are a valid approximation for the more complex orthorhombic phase due to the relatively small atomic displacements, only very few studies have actually compared different phases directly [5,16]. Therefore, further efforts to examine the validity of this claim are highly desirable. The objective of this work is to provide such a systematic comparison of the atomic structure, electronic energy bands, and optical properties of these three most relevant phases of potassium niobate, based on state-of-the-art first-principles calculations.

An important prerequisite for quantitative predictions of optical properties is a reliable electronic band gap. Although standard density-functional theory is capable of yielding highly accurate atomic structures, it is also known to systematically underestimate band gaps. One common way to overcome this flaw is to use hybrid density functionals that incorporate a certain amount of nonlocal exact exchange as in Hartree-Fock calculations [16,17]. This approach is not entirely satisfactory, however, because of the partially empirical nature of hybrid density-functional theory, which leaves some arbitrariness in choosing the mixing parameter and thereby limits the explanatory power of the results. Even if the amount of exact exchange is fixed to match the experimentally measured band gap, as is often done in practice, the problem does not vanish, because experimental values usually refer to the optical band gap instead of the electronic transport gap

───────────
[*]Corresponding author: schmidtf@mail.upb.de

[18–23]. It is unknown how large the deviation between the electronic and the optical band gap is in the case of potassium niobate, but for the very similar lithium niobate ($LiNbO_3$), a significant discrepancy has been found [24,25]. As an alternative, we employ Hedin's *GW* approximation [26] to include quasiparticle effects in the electronic band structure in this work. This approach yields band gaps in very good agreement with experimental photoemission measurements for a wide range of materials [27] and has already been successfully applied to lithium niobate [28,29]. To our knowledge, no *GW* calculations have been reported for potassium niobate so far, however.

In addition to the electronic band structure, we examine the influence of many-body effects, such as electron-hole attraction and local-field effects, on the linear optical absorption spectrum by solving the Bethe-Salpeter equation (BSE). This goes beyond previous results for $KNbO_3$ obtained with a lower level of approximation [16] and should improve the agreement with experimental data.

Arguably the most important property of potassium niobate is its large optical nonlinearity, which makes this material interesting for many technological applications. However, there is surprisingly little actual data, because typical experiments merely probe the nonlinear susceptibility at single laser frequencies, usually at 1064 nm [30–33]. Even many theoretical studies follow this lead and only give the nonlinear susceptibility at certain discrete frequencies [34–36]. In order to extend our knowledge of the nonlinear optical response, we both measure and calculate the nonlinear susceptibility over a larger frequency range in this work.

As the structural differences between the phases are rather small, special emphasis must be placed on finding the best geometrical data possible. Therefore, after describing our computational and experimental methods in Sec. II, we test different exchange-correlation functionals in Sec. III A and compare our results with available experimental data. In Sec. III B, the influence of quasiparticle corrections on the electronic band structure is analyzed. In Secs. III C and III D we then study the linear and nonlinear optical properties of potassium niobate based on the frequency-dependent linear dielectric function and the nonlinear susceptibility for second-harmonic generation, respectively. Finally, Sec. IV summarizes our conclusions.

II. METHODS

A. Computational approach

All calculations reported in this work are carried out with the Vienna *Ab initio* Simulation Package (VASP) [37], a plane-wave implementation of density-functional theory (DFT). Specifically, we employ the projector-augmented-wave formalism [38] together with pseudopotentials optimized for *GW* calculations to describe the electron-ion interaction. In a recent preliminary study [17], we already compared the performance of several exchange-correlation functionals for $KNbO_3$ and found that the PBEsol functional [39], a revised version of the popular Perdew-Burke-Ernzerhof (PBE) generalized gradient approximation (GGA) [40], reproduced the experimental lattice parameters across the different phases satisfactorily and better than any of the considered

alternatives. Nevertheless, we choose to carry out further testing here by extending our comparison to the so-called strongly constrained and appropriately normed (SCAN) functional [41], a meta-GGA that was recently claimed to be particularly accurate for ferroelectric materials [42].

For the structure optimization within DFT, we use an energy cutoff of 600 eV for the plane-wave basis set, which is raised with respect to the default cutoffs for the pseudopotentials in order to eliminate the Pulay stress, and a mesh of $6 \times 6 \times 6$ **k** points to sample the Brillouin zone, which corresponds to a primitive real-space unit cell with the same number of atoms for all three phases. The ionic relaxation is performed by calculating the stress tensor and allowing all external and internal degrees of freedom to change until the forces are smaller than 0.001 eV/Å. These parameter values are the same as in our previous study [17] and ensure well converged structures.

The quasiparticle band structures within the *GW* approximation are obtained using the implementation of Shishkin and Kresse [43,44]. We include a certain degree of self-consistency by iteratively updating the eigenvalues in the Green function *G* used in the construction of the self-energy, but not the eigenfunctions or the dynamically screened Coulomb interaction *W* [44,45]. In a previous study [29] we found that this approach, known nowadays as eigenvalue self-consistent *GW* (evGW_0), yields particularly accurate quasiparticle band structures in the case of $LiNbO_3$. For the evGW_0 calculations, we use a plane-wave cutoff of 200 eV for the response function, a $8 \times 8 \times 8$ **k**-point mesh, and a total of 384 electronic energy bands. Wannier interpolation [46] is employed to improve the sampling of the Brillouin zone. These numerical parameters are chosen to ensure a convergence of the evGW_0 eigenvalues to better than 0.1 eV.

Subsequently, the Bethe-Salpeter equation (BSE) is solved to account for the electron-hole attraction and local-field effects in the linear optical spectra. To reduce the numerical cost, we employ the Tamm-Dancoff approximation; many studies, including Refs. [47–50], have shown that this approximation has only a small effect on the optical absorption spectrum and yields almost the same results as the diagonalization of the full BSE matrix. We use the implementation of Schmidt *et al.* [51] and first obtain the imaginary part of the dielectric function numerically in a finite frequency interval. The real part is derived by means of the Kramers-Kronig relation from the imaginary part, which is extended with an analytic high-frequency tail for this purpose as described by Adolph *et al.* [52]. All electronic states within a distance of 15 eV from the Fermi energy are included, and the **k** mesh is increased to $12 \times 12 \times 12$ points for the linear optical properties. As standard DFT calculations typically yield significantly too small band gaps, quasiparticle or scissors shifts deduced from the preceding evGW_0 calculations are applied to widen the band gap.

The components of the nonlinear susceptibility, which are relevant for second-harmonic generation (SHG), are determined within the independent-(quasi)particle approximation following the approach of Leitsmann *et al.* [53]. In this step, we use a dense **k** mesh with $16 \times 16 \times 16$ points, and include all states within the energy window from 40 eV below to 30 eV above the Fermi energy. Although the peak positions

of the nonlinear susceptibility are entirely determined by electronic transitions up to twice the incident frequency, the oscillator strengths in the three-body contribution to the susceptibility involve a summation over all valence and conduction states [25]. The chosen energy window yields well-converged spectra in Sec. III D below, where the nonlinear susceptibility is shown up to an incident frequency of 8 eV.

B. Experimental setup

The analyzed samples are commercially available orthorhombic stoichiometric $KNbO_3$ crystals [Forschungsinstitut für mineralische und metallische Werkstoffe Edelsteine/Edelmetalle GmbH (FEE) that were polished for a smooth surface]. The components of the nonlinear optical susceptibility $\chi^{(2)}$ are determined at room temperature by a broadly tunable titanium-sapphire laser (Spectra Physics Tsunami HP) providing 80–150 fs pulses at a repetition rate of 78 MHz ranging from 720 to 1080 nm. Accordingly, the pulse energies lie between 10 and 35 nJ. The accessible wavelength range is extended by doubling the fundamental frequency using a commercially available BBO crystal. The light is focused on the sample with an appropriate achromatic doublet lens and is collected similarly. The collimated beam is spectrally dispersed in a rotatable prism to separate the different orders, and the SHG is detected by a gallium phosphide photodiode. A current-voltage preamplifier (Stanford SR570) and a lock-in amplifier (Stanford SR830) are used to ensure a good signal-to-noise ratio. Alternatively, all orders can be detected by a Czechy-Turner spectrometer equipped with a deep-depletion silicon charge-coupled-device array sensor (Andor DU440) to evaluate the complete spectrum of the emission in order to identify higher-order nonlinear processes that could affect the efficiency measurements. All experiments are performed with a synchronous reference in a symmetric two-beam geometry to account for any changes in pulse durations and energies, i.e., by using identical amounts of reflective surfaces, focusing optics, and optical path lengths. The sample is mounted under normal incidence in one branch and a z-cut quartz crystal is used for reference in the other, correcting the data for its known absolute value of $d_{11} = 0.3$ pm/V at 1064 nm [54]. We use Miller's constant-delta condition [55] with a Miller delta of $\delta_{11} = 1.328 \times 10^{-2}$ m/C to account for the dispersion of the second-order nonlinear coefficient of the quartz reference; the Miller delta is calculated from the d_{11} value and the refractive index at 1064 nm [56]. Reflection measurements for $KNbO_3$ are performed in a commercially available UV-VIS-NIR spectrophotometer (Perkin Elmer L900) in reflection mode.

III. RESULTS AND DISCUSSION

A. Structure optimization

In this work we focus on the orthorhombic phase of $KNbO_3$, which is stable at room temperature and hence of central interest for technological applications, as well as the structurally simpler cubic and tetragonal phase that often serve as test systems in theoretical simulations. The cubic phase displayed in Fig. 1(a) has only one independent lattice
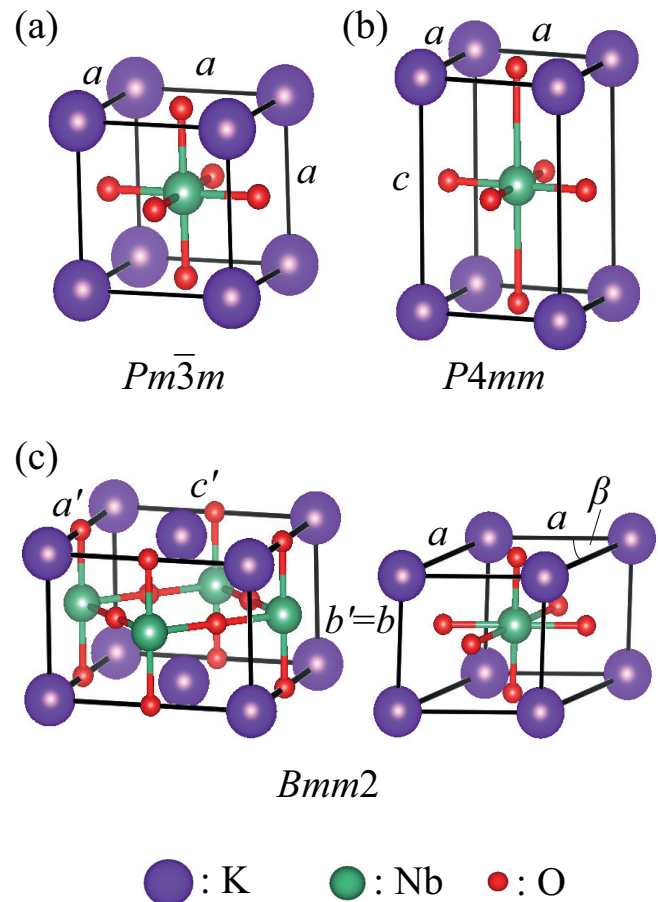

FIG. 1. Different phases of $KNbO_3$: (a) cubic, (b) tetragonal, and (c) orthorhombic (left: conventional orthorhombic unit cell, right: primitive rhombic unit cell) with lattice parameters, angles, and space groups in Hermann-Mauguin notation. The deformations are actually very small and are exaggerated here for clarity.

parameter a, while the tetragonal phase shown in Fig. 1(b) has two distinct lattice parameters a and c. In both cases, the three crystal axes are perpendicular. The orthorhombic phase shown in Fig. 1(c) can be represented using either the conventional orthorhombic cell (left), which contains two formula units of $KNbO_3$, or the primitive rhombic cell (right), which contains one formula unit. While the conventional orthorhombic cell has three perpendicular lattice vectors of distinct length a', b', and c', two lattice vectors of the primitive cell are of equal length but enclose an obtuse angle β.

As all known phases of $KNbO_3$ are structurally nearly degenerate, a very careful relaxation is necessary, and extensive testing of different exchange-correlation functionals seems appropriate to ensure robust results. Therefore, we test the GGA functionals PBE and PBEsol as well as the SCAN meta-GGA functional for the three principal phases considered here. Table I shows the calculated lattice parameter and the associated unit-cell volume for the cubic phase together with experimental data by Shirane *et al.* [57] and by Fontana *et al.* [5]. At first sight, the PBE results appear to be the closest match, but one must keep in mind that the experiments

TABLE I. Lattice parameter a and equilibrium unit-cell volume V obtained with the PBE, SCAN, and PBEsol exchange-correlation functionals for the cubic phase of $KNbO_3$ together with available experimental values.

	PBE	SCAN	PBEsol	Expt. [57]	Expt. [5]
a (Å)	4.024	3.987	3.985	4.0214	4.022
V (Å^3)	65.16	63.39	63.28	65.03	65.06

were performed at 698 and 708 K, respectively, while our calculations correspond to 0 K and do not account for the thermal lattice expansion. Indeed, if the lattice parameter a of the cubic phase measured at different temperatures in [57] is extrapolated to 0 K based on linear regression, one obtains a limiting value of 3.990 Å, in good agreement with the SCAN and PBEsol results.

While the ideal perovskite structure of cubic $KNbO_3$ is centrosymmetric and hence paraelectric, the transition to the tetragonal phase is accompanied by internal atomic displacements along the c axis that break the inversion symmetry and give rise to a ferroelectric polarization. In the notation of Hewat [58], the K atom is positioned at $(0, 0, \Delta(K))$, the Nb atom at $(\frac{1}{2}, \frac{1}{2}, \frac{1}{2} + \Delta(Nb))$, and the three O atoms at $(\frac{1}{2}, \frac{1}{2}, \Delta(O_I))$, $(\frac{1}{2}, 0, \frac{1}{2} + \Delta(O_{II}))$, and $(0, \frac{1}{2}, \frac{1}{2} + \Delta(O_{II}))$ inside the tetragonal unit cell; O_I refers to the oxygen atom in the potassium layer and O_{II} to the two equivalent oxygen atoms in the niobium layer as illustrated in Fig. 1(b). During the structure relaxation, we keep the Nb atom fixed, which constrains $\Delta(Nb) = 0$, while all other atoms are allowed to shift along the c axis. Our results given in Table II show that PBEsol yields lattice parameters in best agreement with the experimental data, considering that the measurements were performed at 543 K under the influence of thermal expansion; if the lattice parameters of the tetragonal phase measured at different temperatures in [57] are linearly extrapolated to 0 K, values of 3.973 and 4.053 Å are obtained for a and c, respectively. The atomic displacements differ between the three functionals but are overall in similarly good agreement with the experimental data.

In the orthorhombic phase, which also exhibits a ferroelectric distortion, atomic displacements occur in a two-

TABLE II. Lattice parameters a and c, ratio c/a, equilibrium unit-cell volume V, and atomic displacements along the c direction obtained with the PBE, SCAN, and PBEsol exchange-correlation functionals for the tetragonal phase of $KNbO_3$ together with available experimental values.

	PBE	SCAN	PBEsol	Expt. [58]
a (Å)	3.994	3.968	3.969	3.997
c (Å)	4.193	4.086	4.058	4.063
c/a	1.0498	1.0296	1.0224	1.0165
V (Å^3)	66.87	64.34	63.93	64.91
$\Delta(K)$	0.01762	0.01621	0.01462	0.018
$\Delta(Nb)$	0	0	0	0
$\Delta(O_I)$	0.06142	0.04838	0.04109	0.044
$\Delta(O_{II})$	0.04962	0.04266	0.03850	0.040

TABLE III. Atomic positions with respect to the conventional orthorhombic unit cell as fractions of a', b', and c'.

K	0	0	$\Delta_z(K)$
K	$\frac{1}{2}$	0	$\frac{1}{2} + \Delta_z(K)$
Nb	0	$\frac{1}{2}$	$\frac{1}{2} + \Delta_z(Nb)$
Nb	$\frac{1}{2}$	$\frac{1}{2}$	$\Delta_z(Nb)$
O_I	0	0	$\frac{1}{2} + \Delta_z(O_I)$
O_I	$\frac{1}{2}$	0	$\Delta_z(O_I)$
O_{II}	$\frac{1}{4} + \Delta_y(O_{II})$	$\frac{1}{2}$	$\frac{3}{4} + \Delta_z(O_{II})$
O_{II}	$\frac{3}{4} - \Delta_y(O_{II})$	$\frac{1}{2}$	$\frac{3}{4} + \Delta_z(O_{II})$
O_{II}	$\frac{1}{4} - \Delta_y(O_{II})$	$\frac{1}{2}$	$\frac{1}{4} + \Delta_z(O_{II})$
O_{II}	$\frac{3}{4} + \Delta_y(O_{II})$	$\frac{1}{2}$	$\frac{1}{4} + \Delta_z(O_{II})$

dimensional plane. In Table III we list the atomic positions with respect to the conventional orthorhombic unit cell, following once more the notation of Hewat [58]. The oxygen atoms in the niobium layer, but not those in the potassium layer, are subject to sideward displacements along the a' direction. In addition, all atoms shift along the c' direction. During the structure relaxation we again keep the niobium atoms fixed, which leaves four independent dimensionless internal parameters to be optimized simultaneous with the three external lattice parameters.

Table IV shows our results for the orthorhombic phase calculated with the PBE, SCAN, and PBEsol functional together with available data from other authors for comparison. On the experimental side, we include data from single-crystal x-ray measurements by Katz and Megaw [59] and from powder diffraction by Hewat [58], both at room temperature. Zhang *et al.* [22] also recently measured the displacements using annular-bright-field scanning transmission electron microscopy (ABF-STEM) and obtained results in good agreement with the earlier experimental measurements. Additionally, they performed spin-polarized DFT calculations based on the Wu-Cohen exchange-correlation functional. No values for the external lattice parameters are reported in [22], but the atomic displacements, shown in Table IV for comparison, are in good agreement with our numerical results. Comparing the three functionals, we observe that PBEsol predicts the ratios a'/b' and c'/b' with the highest accuracy. The absolute values of the lattice parameters are slightly underestimated, however, which can again be attributed in part to thermal expansion, as the experiments were performed at room temperature. As an estimate, we convert the measured lattice parameters given for the primitive rhombic unit cell in [57] to the orthorhombic cell and linearly extrapolate these to 0 K, which yields the limiting values 5.697, 3.950, and 5.727 Å for a', b', and c', respectively. It should be noted that the measured values for a' and c' exhibit very little variation, while b' and the unit-cell volume shrink with decreasing temperature; the latter extrapolates to 128.85 Å^3 at 0 K. In addition to highly accurate lattice parameters, SCAN predicts the atomic displacements in best agreement with the experiments, although the actual quantitative deviation from PBEsol is not large. Finally, PBE yields lattice parameters that even exceed the experimental values and is clearly inferior to the other two functionals.

TABLE IV. Lattice parameters a', b', and c', ratios a'/b' and c'/b', equilibrium unit-cell volume V, and atomic displacements obtained with the PBE, SCAN, and PBEsol exchange-correlation functionals for the orthorhombic phase of KNbO$_3$, together with available experimental and theoretical values for comparison.

	PBE	SCAN	PBEsol	Expt. [59]	Expt. [58]	DFT (WC) [22]
a' (Å)	5.782	5.698	5.679	5.697	5.695	–
b' (Å)	3.983	3.958	3.961	3.971	3.973	–
c' (Å)	5.816	5.723	5.696	5.720	5.721	–
a'/b'	1.4517	1.4396	1.4337	1.4347	1.4335	–
c'/b'	1.4602	1.4459	1.4380	1.4404	1.4402	–
V (Å^3)	133.94	129.07	128.11	129.42	129.44	–
Δ_z(K)	0.01550	0.01402	0.01236	0.017	0.0138	0.007
Δ_z(Nb)	0	0	0	0	0	0
Δ_z(O$_I$)	0.04160	0.03683	0.03261	0.021	0.0364	0.026
Δ_z(O$_{II}$)	0.03915	0.03399	0.03008	0.035	0.0342	0.022
Δ_y(O$_{II}$)	0.00542	0.00347	0.00190	0.004	0.0024	0.001

From our results, we conclude that PBEsol is very well suited to describe the orthorhombic phase as well as the simpler cubic and tetragonal phase of KNbO$_3$, and that there is overall no advantage in using SCAN in this case. Therefore, we use optimized crystal structures obtained with the PBEsol functional for all phases in the following if not stated otherwise.

B. Band structures

To examine the influence of quasiparticle effects, the band structure of KNbO$_3$ is evaluated both within DFT and within the evGW_0 approximation. As explained in the previous section, we use the geometries obtained with the PBEsol functional, which are in very good agreement with the available experimental data throughout the different phases. As PBEsol is specifically designed for structure optimization but in general performs worse for total or atomization energies [39], the band structures themselves are here determined with the PBE functional, although our tests indicate that the results would actually be almost identical for KNbO$_3$ if PBEsol were used in this step.

Table V summarizes the band gaps calculated with the PBE functional in the context of DFT and with the evGW_0 approximation for the electronic self-energy. The direct band gap refers to the distance between the valence and conduction band edges at the Γ point, whereas the indirect band gap refers to the distance between the valence-band maximum and the conduction-band minimum. Compared to PBE, the evGW_0 quasiparticle shifts widen the direct (indirect) band gap by

1.21 (1.44), 1.58 (1.55), and 1.67 (1.64) eV for the cubic, tetragonal, and orthorhombic phase, respectively.

Many experiments have been carried out to determine the direct band gap of KNbO$_3$, reporting results of 3.14 [19], 3.16 [20], and 3.24 eV [21] for the cubic, 3.08 [21] and 3.30 eV [18] for the tetragonal, and 3.15 [21], 3.17 [23], and 3.25 eV [22] for the orthorhombic phase. In line with earlier theoretical studies at the same level of approximation, such as [60], our PBE results substantially underestimate the measured band gaps for all three phases, a well-known drawback of DFT calculations with local or semilocal exchange-correlation functionals. The evGW_0 approximation is much closer to the experimental values, but it must be kept in mind that our calculations refer to the electronic band gaps while the experimental data refer to optical band gaps, which are additionally affected by electron-hole attraction. Systematic deviations are therefore expected. Indeed, for the closely related LiNbO$_3$, the electronic and optical band gap are known to differ significantly [29]. In the following section we solve the Bethe-Salpeter equation to take the missing excitonic effects in the optical absorption of KNbO$_3$ into account. The electron-phonon coupling, which is presently ignored in our calculations, is also expected to have an influence; in the case of LiNbO$_3$, even the temperature-independent zero-point renormalization alone reduces the band gap by several tenths of an eV [61].

The results shown in Table V indicate that the evGW_0 quasiparticle corrections increase the direct and indirect band gap by a similar amount, especially for the tetragonal and the orthorhombic phase, although the two band-gap values refer to transitions between different electronic eigenstates. This is further corroborated by Fig. 2, which shows the full band structure for the orthorhombic phase and confirms that the dispersion of the valence and conduction bands is almost identical at both levels of approximation. The conduction bands are shifted towards higher energies in the evGW_0 calculation, however. From this observation, we infer that the inclusion of quasiparticle effects changes the form of the band structure only to an insignificant degree and mostly widens the band gap. This suggests the use of a scissors operator for optical-response calculations that require a dense

TABLE V. Direct and indirect band gaps of cubic, tetragonal, and orthorhombic KNbO$_3$ calculated within PBE and within the evGW_0 approximation. All values are in eV.

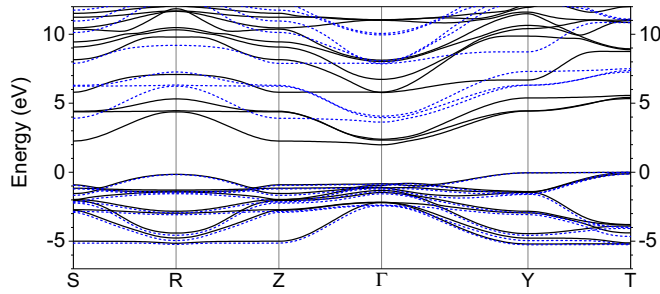|	Cubic	Tetragonal	Orthorhombic
PBE direct	2.40	2.48	2.82
PBE indirect	1.75	1.65	1.99
evGW_0 direct	3.61	4.06	4.49
evGW_0 indirect	3.19	3.20	3.63

FIG. 2. Band structure in the Brillouin zone corresponding to the primitive unit cell of the orthorhombic phase calculated with the PBE functional (black solid lines) and with evGW_0 quasiparticle shifts (dashed blue lines).

k-point mesh. The scissors shifts used in this work are derived from the quasiparticle correction of the direct band gaps and amount to 1.21, 1.58, and 1.67 eV for the cubic, tetragonal, and orthorhombic phase, respectively.

C. Dielectric function

We now turn to the linear optical properties of KNbO$_3$. Several methods to construct the dielectric function are compared for the orthorhombic phase in Fig. 3: A pure DFT-PBE calculation that takes only transitions between single-particle eigenstates into account (black line), the same with a rigid scissors shift based on the evGW_0 approximation (blue line, top) and with individually calculated evGW_0 quasiparticle shifts for all eigenstates (blue line, bottom), as well as the solution of the BSE in combination with a scissors shift (red line, top) and with individual quasiparticle shifts (red line, bottom). In all cases, the same crystal structure obtained from PBEsol is used. The theoretical results are furthermore compared to experimental data (gray line) from [7].

The fact that the scissors and quasiparticle shifts yield almost identical results, both at the single-particle level and in the context of the BSE, supports our earlier statement that the evGW_0 self-energy correction mainly serves to widen the band gap and may be replaced by a numerically less costly scissors shift for practical purposes. While the pure PBE results are significantly too low in energy, reflecting the too small band gap, the inclusion of quasiparticle effects and the consequent widening of the band gap cause a strong blueshift, beyond the measured position of the optical spectrum. Finally, if the BSE is solved, then the spectrum is slightly redshifted again, in good alignment with the experimental data. Furthermore, a marked redistribution of oscillator strength can be observed in the BSE results: Whereas the first peak in the imaginary part of the dielectric function is followed by larger peaks at the DFT and evGW_0 level of theory, this first resonance dominates in the BSE results, in agreement with the experiment. This behavior is typical for excitonic resonances in solids and found in many materials, including LiNbO$_3$ [24].

Based on the position of the first peak in the imaginary part of the PBE and BSE spectra, both with identical scissors shifts, we estimate an exciton binding energy of 0.5 eV for the orthorhombic phase. Following the same procedure, we obtain exciton binding energies of 0.6 and 0.5 eV for the cubic and tetragonal phase, respectively. While these values may
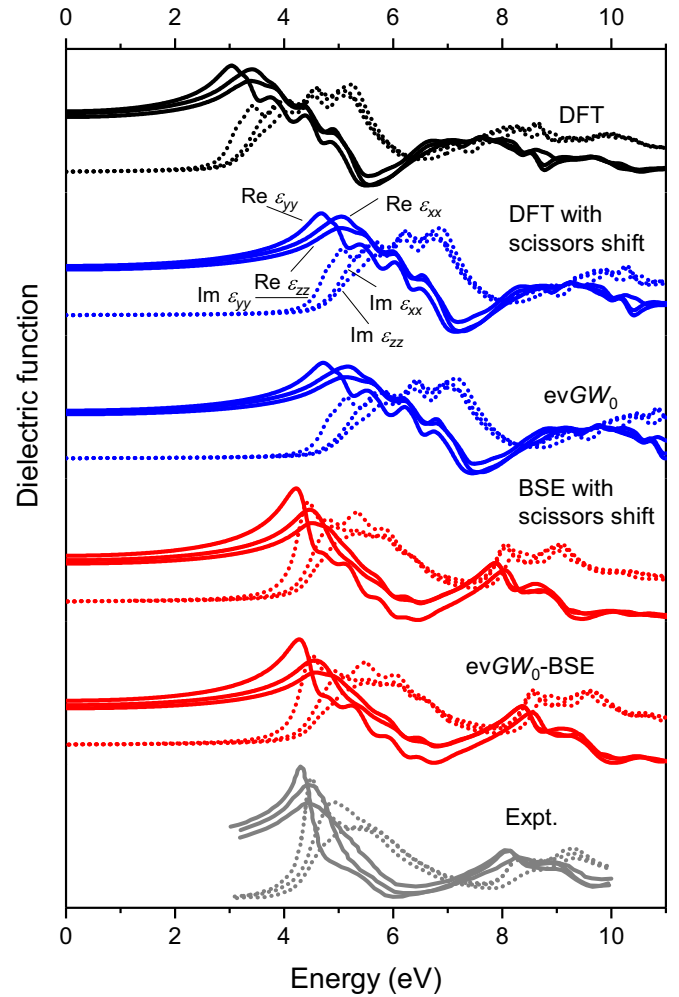

FIG. 3. Real (solid lines) and imaginary parts (dotted lines) of the linear dielectric function of orthorhombic KNbO$_3$ calculated with different methods (top to bottom: DFT, DFT with scissors shift, evGW_0, BSE with scissors shift, evGW_0-BSE). The experimental data (gray lines) are taken from [7].

appear large at first glance, they are of similar magnitude as in LiNbO$_3$ [29].

As the explicit comparison for the orthorhombic phase suggests that the state-dependent evGW_0 quasiparticle shifts can be replaced by a scissors operator for the optical response without noticeable loss of accuracy, we use the latter approach for all subsequent calculations. Figure 4 displays our BSE results obtained in this way for the cubic (top), tetragonal (middle), and orthorhombic phase (bottom). As all three lattice vectors of the cubic phase are perpendicular and of equal length, there is only one independent component of the dielectric function in this case. In contrast, the tetragonal phase features two independent components. The first, dominant resonance in the real part of the *xx* and *yy* component exhibits a double peak, as opposed to the single sharp peak seen in the cubic structure, while the first resonance in the *zz* component is shifted to considerably higher energies. As a consequence, we observe a rather large splitting between the two components. In the orthorhombic phase, there are three independent components, each with a distinct height and
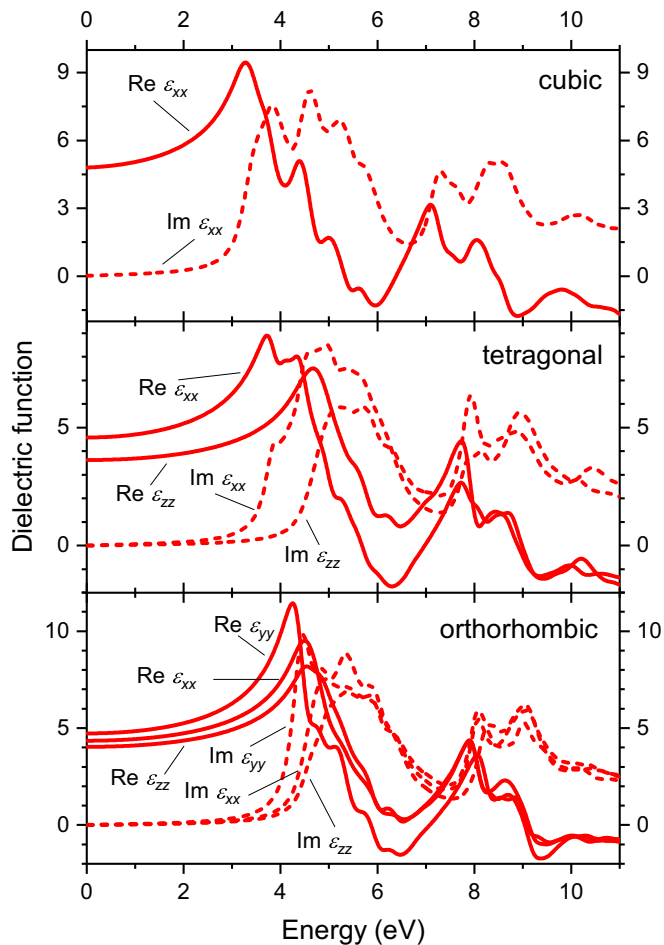
FIG. 4. Real (solid red lines) and imaginary (dotted red lines) parts of the dielectric function for cubic (top), tetragonal (middle), and orthorhombic (bottom) $KNbO_3$ calculated from the BSE with a scissors shift.
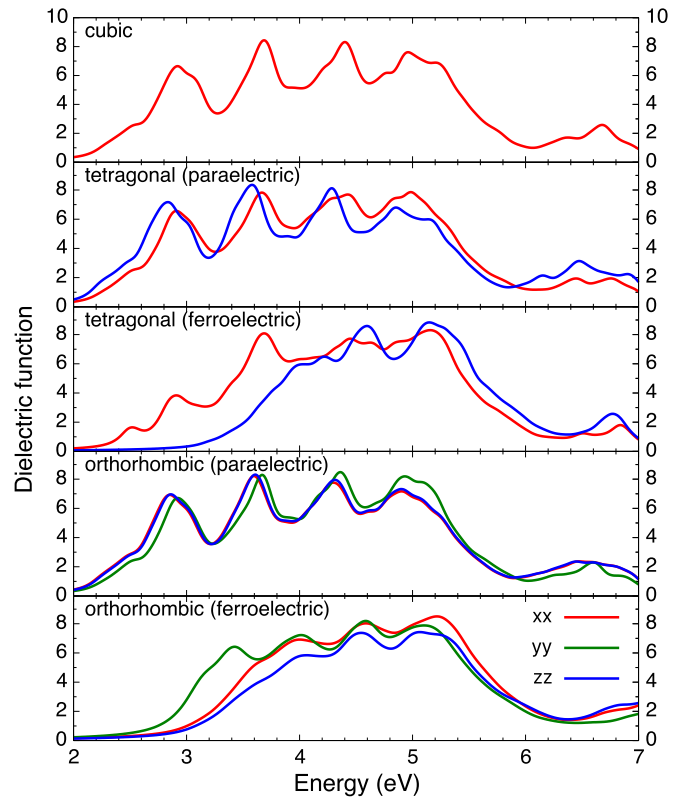

FIG. 5. Components of the imaginary part of the dielectric function for the (top to bottom) cubic, paraelectric tetragonal, ferroelectric tetragonal, paraelectric orthorhombic, and ferroelectric orthorhombic phase calculated within DFT.

position of the first peak in the real part. The splitting is overall smaller than in the tetragonal phase.

Compared to the dielectric function of the orthorhombic phase, we find that the spectrum of cubic (tetragonal) $KNbO_3$ is redshifted by about 1 eV (0.5 eV). Altogether there are many similarities between the three phases, however: The real part always features a dominant peak at around 4 eV and a broader resonance at around 8 eV, while the imaginary part has two broad resonances near 5 and 9 eV. The general shape of the dielectric function is also very similar in all cases. This resemblance is no coincidence but should be expected, since the actual structural differences between the phases are small.

In addition to the experimental data included in Fig. 3, we can compare our results with a recent theoretical study by Xu *et al.* [16], who calculated the linear dielectric function of tetragonal and orthorhombic $KNbO_3$ at the single-particle level using the HSE06 functional. This hybrid functional adds 25 percent of nonlocal exact exchange to a DFT calculation, which widens the band gap and can be interpreted as an approximate static self-energy correction. As the electron-hole attraction as well as local-field effects are neglected, this approach can be compared to our DFT calculations with a

scissors shift (second from top in Fig. 3). Indeed, our results at this level of approximation resemble those of Xu *et al.*, including the general form of the resonances, the double-peak structure of the first resonance in the real part of ε_{xx} and ε_{yy} for the tetragonal phase, and the larger splitting in the tetragonal compared to the orthorhombic phase. There are some differences, however. In particular, our calculations predict the splitting between the three independent components for the orthorhombic phase in better agreement with the experimental data [7]. Furthermore, the redshift that we find in the spectrum of the tetragonal relative to the orthorhombic phase is absent in [16]. This is likely related to the different underlying band gaps: From our evGW_0 results listed in Table V, we obtain a deviation of 0.43 eV between the two phases, while Xu *et al.* report a deviation of only 0.05 eV for the indirect band gap based on HSE06. The smaller band gap of the tetragonal phase in our calculations consequently shifts the spectrum towards lower energies.

In order to gain more insight into the splittings and the shifts of the spectral features, we further analyze the dielectric function of cubic, tetragonal, and orthorhombic $KNbO_3$ in Fig. 5 at the level of DFT, where spectral resonances can be directly related to electronic transitions between valence and conduction bands. For the tetragonal and orthorhombic phase, we consider not only the stable ferroelectric structures obtained from the unconstrained ionic relaxation in Sec. III A, which involves symmetry-breaking displacements of atoms
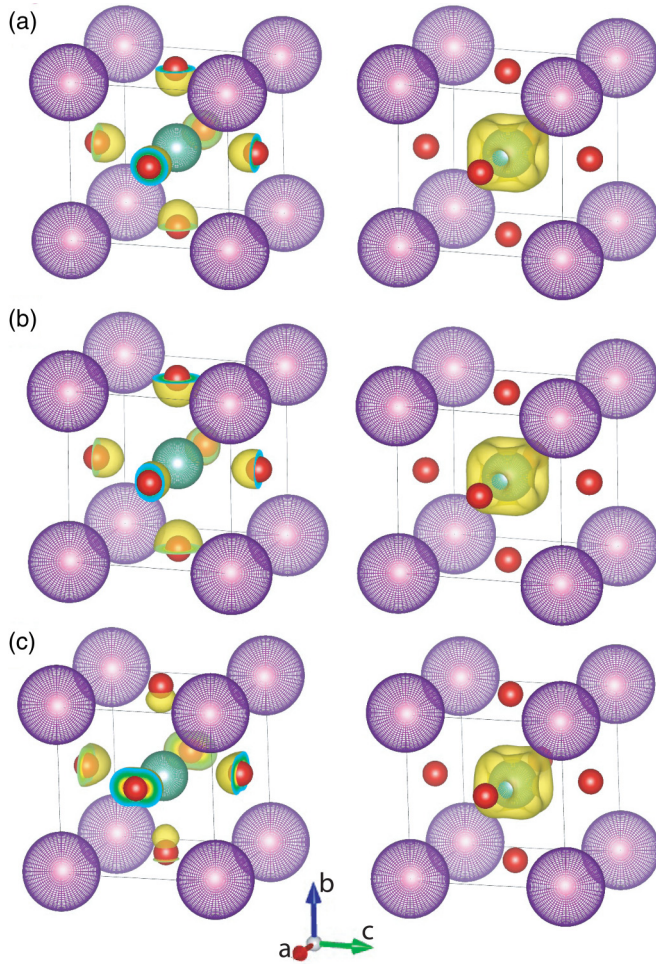
TABLE VI. Calculated direct band gaps for the cubic phase of $KNbO_3$ and for the tetragonal and orthorhombic phase in the paraelectric (p) and ferroelectric (f) configuration within DFT-PBEsol (including evGW_0 quasiparticle shifts) at high-symmetry points in the Brillouin zone. All values are in eV.

k	Cubic	Tetr. (p)	Tetr. (f)	Orth. (p)	Orth. (f)
X	2.55 (4.06)	2.49	3.47 (5.16)	3.53	3.96 (5.77)
Y	2.55 (4.06)	2.49	3.47 (5.16)	2.49	3.57 (5.32)
Z	2.55 (4.06)	2.55	2.56 (4.18)	3.54	4.07 (5.89)

FIG. 6. Band-decomposed charge density (yellow) of the three highest valence bands (left) and the three lowest conduction bands (right) of $KNbO_3$ for the cubic phase (a) and tetragonal phase in the paraelectric (b) and ferroelectric (c) configuration. Potassium, niobium, and oxygen atoms are indicated by large purple, medium green, and small red balls, respectively.

Figure 6 illustrates the band-decomposed charge densities for the cubic phase and for the tetragonal phase in the paraelectric and ferroelectric configuration. We observe that the highest valence bands originate from oxygen p orbitals, while the lowest conduction bands originate from niobium d orbitals, in line with the density of states reported earlier [17].

While the charge density of the lowest conduction bands is insensitive to the structural details in Fig. 6, we find a marked difference in the charge density of the highest valence between the cubic phase and the tetragonal phase in the paraelectric configuration on the one hand and the stable ferroelectric configuration of the tetragonal phase on the other: In the latter case, the charge density at the oxygen atoms in the potassium layer clearly differs from that at the two equivalent oxygen atoms in the niobium layer. Similar observations can be made for the orthorhombic phase, where the principal changes to the charge densities also arise from the ferroelectric polarization rather than the deformation of the unit cell.

The symmetry lowering associated with the successive structural modifications is accompanied by a lifting of degeneracies in the electronic band structure, especially with regard to the oxygen p orbitals, as illustrated by the direct gaps at X, Y, and Z in the first Brillouin zone listed in Table VI. Transitions close to these high-symmetry points are chiefly responsible for the first major peak in the dielectric function. In particular, the direct gap of 2.55 eV in the cubic phase corresponds to the first shoulder at the same energy in Fig. 5(a). There is no splitting, as all faces of the cubic Brillouin zone are equivalent.

For the tetragonal phase, the small difference of merely 0.06 eV between the direct gaps at X and Z for the paraelectric configuration explains the minor splitting of the two components in Fig. 5(b). While the gap at Z is nearly the same for the ferroelectric configuration, the gap at X is drastically enlarged. The resulting deviation of 0.91 eV and the enhanced anisotropy of the electronic structure are reflected in the large blueshift of the zz component relative to the xx component seen in Fig. 5(c).

Due to the further symmetry reduction, the dielectric function has three distinct components in the orthorhombic phase. In the paraelectric configuration, the xx and zz components displayed in Fig. 5(d) are almost indistinguishable, however. This very weak lateral anisotropy is also reflected in the nearly identical gaps at X and Z. The ferroelectric displacements again enhance the anisotropy, leading to larger deviations between the different high-symmetry points in combination with increased absolute values of the band gaps. Consequently,

from their ideal positions, but also hypothetical paraelectric configurations with identical lattice parameters and no atomic displacements. The latter may be regarded as intermediate states that can be described in terms of a deformation potential tensor applied to the cubic phase. Although the spectral weights differ from the BSE results in Fig. 4, the twofold splitting in the tetragonal phase and the threefold splitting in the orthorhombic phase, including the ordering of the components, as well as the overall blueshift that is stronger for the tetragonal than the orthorhombic phase, are evidently very similar in DFT for the ferroelectric configurations. In contrast, the paraelectric configurations exhibit much smaller splittings and no blueshift, retaining a strong similarity to the cubic phase. This suggests that the internal atomic displacements resulting from the ferroelectric polarization rather than the deformation of the unit cell are responsible for the observed changes in the dielectric function.

From a band decomposition, we further find that the onset of the optical absorption is due to transitions from the three highest valence bands to the three lowest conduction bands.

TABLE VII. SHG components $\chi^{(2)}_{ijk}$ of tetragonal KNbO$_3$ at $\omega = 0$ calculated using geometries optimized with the PBE, SCAN, and PBEsol functional, and the geometry determined experimentally in [58], "sci" indicates if a scissors shift was used. We also include theoretical results by Xue and Zhang [34] from a bond-charge model (BCM) and by Cabuk [36] from DFT-LDA with a scissors shift. All values are in Å/V.

ijk	PBE	SCAN	PBEsol	PBEsol	Hewat	BCM [34]	LDA [36]
sci	yes	yes	yes	no	yes	–	yes
xxz	0.326	0.313	0.308	0.823	0.331	–	0.146
zxx	0.139	0.221	0.278	0.823	0.282	0.251	0.146
zzz	0.484	0.424	0.392	0.818	0.413	0.685	0.355

there is an overall blueshift in Fig. 5(e), and the splitting between the xx and zz component increases.

Comparing the stable ferroelectric configurations of the tetragonal and orthorhombic phase, we finally note that the larger quantitative splitting of the components of the dielectric function observed for the tetragonal phase corresponds to a larger deviation of 0.91 eV between the gaps at X and Z, signaling a stronger anisotropy than for the orthorhombic phase, where the band-gap values in Table VI differ only by 0.50 eV. This reduced splitting further accords with the smaller displacements of the oxygen atoms found in Sec. III A. Therefore, we conclude that the splittings and shifts in the spectra are principally determined by the magnitude of the ferroelectric displacements of the oxygen atoms from their ideal positions rather than the deformation of the unit cell.

The inclusion of quasiparticle shifts at the evGW_0 level leads to larger absolute band gaps but does not change this interpretation. As shown in Table VI for the cubic phase and the two ferroelectric configurations, the quasiparticle shifts are nearly identical at different **k** points in the Brillouin zone, illustrating again the justification of a rigid scissors operator, and furthermore vary only little between the three considered phases.

D. Second-harmonic generation

Next we focus on the nonlinear optical properties. As cubic KNbO$_3$ is centrosymmetric and hence generates no second-order optical response, we start with the tetragonal phase. For computational reasons, we limit ourselves to the independent-(quasi)particle approximation in this section. Table VII shows

the nonvanishing independent components of the static SHG tensor at $\omega = 0$ calculated with different approaches. In order to probe the possible sensitivity to small atomic displacements, we use the optimized geometries obtained from relaxations with the PBE, SCAN, and PBEsol functional, as well as the structure experimentally determined by Hewat [58]. The wave functions used to evaluate the nonlinear susceptibility are obtained with the PBE functional in all cases, so that any deviations in the resulting spectra arise exclusively from the minor differences in the atomic positions. A scissors shift of 1.58 eV is usually employed, but for the PBEsol structure we also show results obtained without any shift. Although there are certain deviations between the calculated values for the various geometries, the scissors shift clearly has the strongest impact on the results.

For comparison, Table VII also shows values from other theoretical studies. Xue and Zhang [34] calculated the nonlinear coefficients from a bond-charge model based on the geometry reported by Hewat [58], while Cabuk [36] employed DFT within the local-density approximation (LDA) in combination with a scissors shift. The latter corresponds most closely to our PBE calculation with a scissors shift, which indeed yields very similar numbers.

In Table VIII we show our results for the SHG tensor of orthorhombic KNbO$_3$ at an energy of 1.16 eV, for which experimental data are available. Besides the optimized geometries obtained with the PBE, SCAN, and PBEsol functional, we also consider the structure determined experimentally by Katz and Hewat [59] as a starting point for SHG calculations. A scissors shift of 1.67 eV is used in all cases. The fact that some components of the SHG tensor vary by a factor of 3 between the different geometries underlines the importance of accurate structural data and thus justifies the efforts made in Sec. III A. Like the values of the lattice parameters, the nonlinear optical coefficients calculated with the SCAN functional typically lie between those from PBE and PBEsol, and PBEsol yields results closest to those obtained with the experimentally measured geometry. This illustrates the consistency between the quality of the structural data and the SHG spectra calculated on this basis.

Complementing our theoretical analysis, we also perform frequency-resolved measurements of the SHG coefficients. A comparison of our calculated spectra with the measured xxz and zzz tensor components in the energy range between 1.2 and 1.6 eV for orthorhombic KNbO$_3$ is displayed in Fig. 7. While this energy window lies inside the nonresonant region of the xxz component, optical nonlinearities are found

TABLE VIII. SHG components $\chi^{(2)}_{ijk}$ of orthorhombic KNbO$_3$ at 1.16 eV calculated using geometries optimized with the PBE, SCAN, and PBEsol functional, and the geometry (Katz) determined experimentally in [59]. A scissors shift is used in all cases. We also include measured values by Baumert [33] as well as theoretical results by Xue and Zhang [34] from a bond-charge model (BCM) and by Duan *et al.* [35] from DFT-LDA. All values are in Å/V.

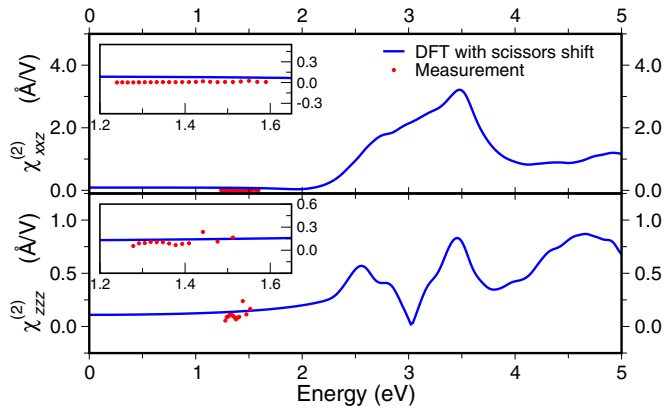| ijk	PBE	SCAN	PBEsol	Katz	Expt. [33]	BCM [34]	LDA [35]
xxz	0.234	0.143	0.086	0.128	0.330	–	–
yyz	0.407	0.407	0.441	0.453	0.342	–	–
zxx	0.612	0.631	0.683	0.596	0.316	0.158	0.663
zyy	0.232	0.357	0.514	0.757	0.366	0.154	0.287
zzz	0.149	0.134	0.127	0.112	0.548	0.433	0.252

FIG. 7. Nonlinear susceptibility of orthorhombic KNbO$_3$ calculated using DFT with a scissors shift (blue lines). The red marks indicate the values measured in this work.

for the *zzz* component. The good overall agreement between theory and experiment illustrates the predictive power of our approach but also demonstrates the importance of self-energy corrections, included here via a scissors shift. Unlike in linear optics, where a scissors shift mainly displaces the spectrum along the energy axis, it also changes the height and form of a resonance significantly in the case of nonlinear optics. This can be seen both in the SHG spectrum of the tetragonal (Fig. 8) and orthorhombic (Fig. 9) phase. By including a scissors shift of 1.58 eV for the tetragonal and 1.67 eV for the orthorhombic phase, the nonlinear susceptibility is reduced to half its value compared to a pure DFT calculation. Furthermore, the relative peak height of a resonance may change. The *zxx* component of the tetragonal phase, for example, exhibits two equally strong resonances at around 2 and 3.5 eV in the pure DFT calculation. With the scissors shift, the first peak is higher than the second, however. These drastic changes caused by a simple scissors shift stress the importance of a reliable underlying quasiparticle correction.

For comparison, Table VIII also shows theoretical results from a bond-charge model by Xue and Zhang [34] and from DFT-LDA calculations by Duan *et al.* [35]. The latter approach is similar to our own, except that no scissors shift was used in [35], while the bond-charge model must be considered more empirical. Furthermore, the table includes measured values taken from Baumert *et al.* [33], which are close to those obtained by other authors [30–32] using various experimental techniques. Overall, our results are in good agreement with the experimental data and predict the magnitude of the second-order nonlinear coefficients correctly. The measured value of the *zzz* component reported in [33] is notably larger than that predicted by our own calculations, as well as larger than found in the other theoretical studies. In particular, Duan *et al.* [35] found the *zzz* component to be smaller than the *zxx* and *zyy* component, in agreement with the present predictions. Additionally, our experimental measurements support the theoretical results for the *zzz* as well as the *xxz* component.

Excitonic effects are presently not included in our SHG calculations for computational reasons. Earlier studies for simpler materials that compared results at the independent-quasiparticle and BSE level [53,62–64] often found an
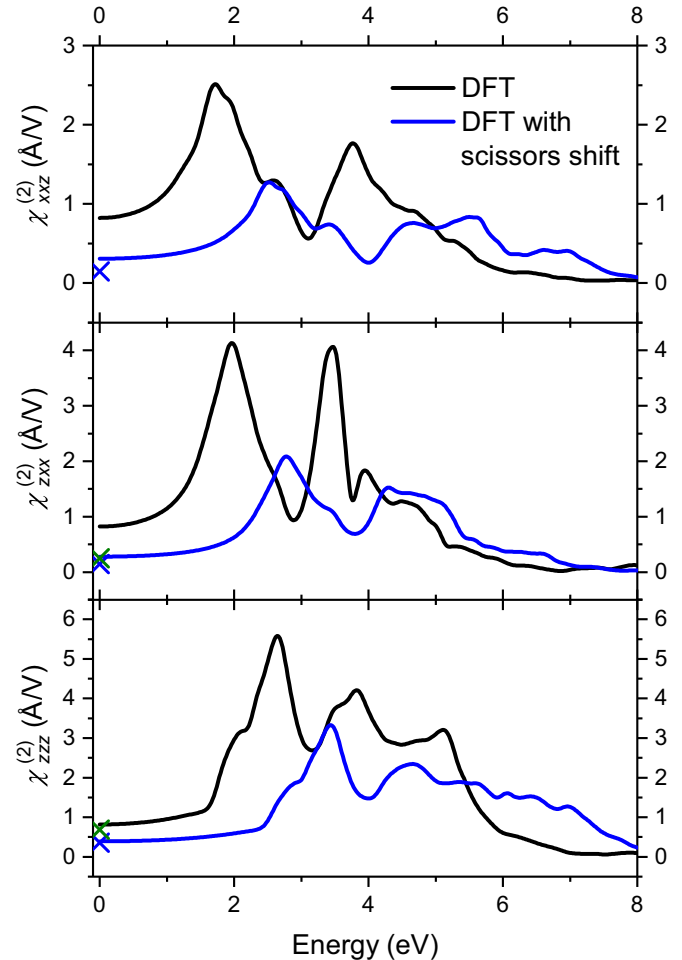

FIG. 8. Nonvanishing components of the nonlinear susceptibility for tetragonal KNbO$_3$ calculated using DFT without (black lines) and with a scissors shift (blue lines), compared to theoretical values from a bond-charge model [34] (green crosses) and from LDA with a scissors shift [36] (blue crosses).

enhancement of the nonlinearities due to excitonic effects. In the case of KNbO$_3$, most measured tensor components of $\chi^{(2)}$ are well reproduced by DFT with a scissors shift, with the exception of the *xxz* and *zzz* component discussed above, where some of the older reported experiments seem to be better described by DFT without a scissors shift. This could be interpreted as an indication for negligible excitonic effects in the SHG data or, in the latter case, as a near cancellation of self-energy and excitonic effects. However, we note that there is not only an appreciable scatter in the experimental data, especially for the *zzz* component, but that these also refer to just a single, relatively low photon energy. In contrast, the novel frequency-dependent measurements performed in this work yield lower values for the nonlinear susceptibility, which are in excellent agreement with the calculations that include quasiparticle effects approximately by means of a scissors operator for both the *xxz* and the *zzz* component. In this way they resolve the previously observed discrepancy. Based on the available experimental data and calculations, sizable excitonic effects can certainly not be excluded, at least not in the energy range of the optical resonances. Further calculations with full
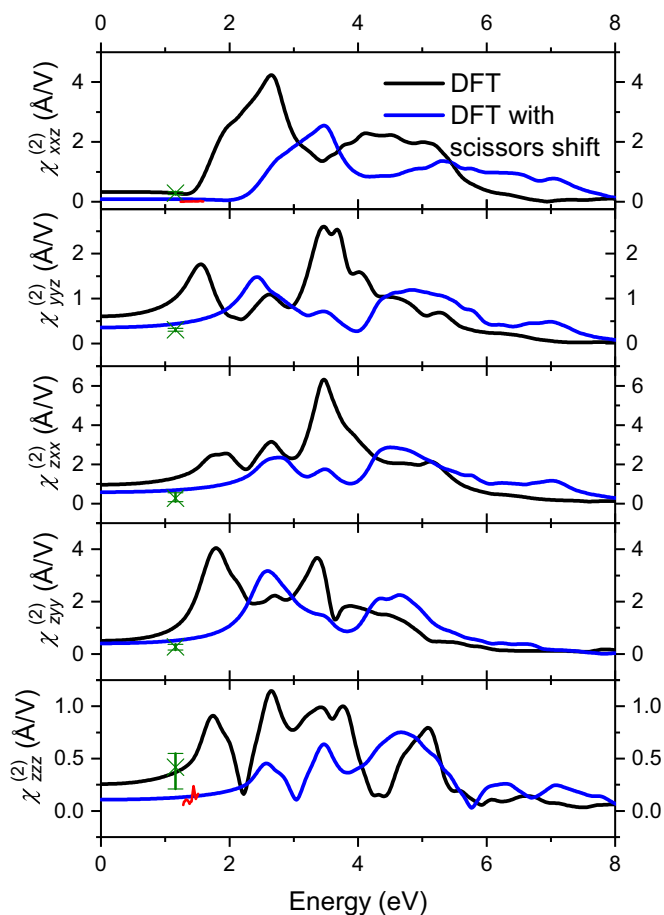
FIG. 9. Nonvanishing components of the nonlinear susceptibility for orthorhombic KNbO$_3$ calculated using DFT without (black lines) and with a scissors shift (blue lines) as well as measurements performed in this work (red lines). The green crosses and brackets indicate the mean value and the spread of the experimental data from [30–35].

inclusion of excitonic effects are thus highly desirable, but out of reach with present numerical capabilities.

IV. CONCLUSIONS

The lattice parameters of the cubic, tetragonal, and orthorhombic phase of KNbO$_3$ were optimized within DFT using the PBE, SCAN, and PBEsol exchange-correlation functional. Although all three functionals lead to reasonable agreement with experimental data, we find that PBEsol performs best on balance and that the results obtained with SCAN typically lie between those from PBE and PBEsol.

Comparing the DFT band structure of orthorhombic KNbO$_3$ with the results from an evGW_0 calculation, we find that the self-energy correction essentially widens the band gap but has little influence on the dispersion of the valence or conduction bands. Thus we conclude that a numerically simpler scissors shift may suffice to give a good description of the electronic structure in optical-response calculations. Indeed, an explicit comparison of the linear dielectric function calculated either with state-dependent quasiparticle shifts or with a rigid scissors shift demonstrates that the results are almost indistinguishable. Besides the self-energy correction

of the electronic eigenstates, the inclusion of excitonic effects, which were ignored in previous theoretical studies of KNbO$_3$, is also essential to achieve good quantitative agreement with experimentally measured spectra. Based on the peak positions in the imaginary part of the dielectric function obtained from the BSE and the independent-quasiparticle approximation, we deduce an exciton binding energy of 0.6, 0.5, and 0.5 eV for the cubic, tetragonal, and orthorhombic phase, respectively.

The dielectric functions for the three considered phases share many similarities regarding the position and form of the resonances in both the real and the imaginary part. The most obvious difference is the splitting between the various components. While the cubic phase exhibits no splitting due to symmetry reasons, there are three distinct components for the orthorhombic phase, albeit with a rather small splitting. The tetragonal phase features the largest splitting between its two distinct components. These splittings result mainly from the lifting of degeneracies of the oxygen p orbitals due to symmetry-breaking displacements of the atoms from their ideal positions in the ferroelectric configurations, whereas the shape deformation of the unit cell has only a minor influence. Furthermore, the spectrum for the tetragonal (cubic) phase is shifted by about 0.5 eV (1 eV) towards smaller energies compared to the orthorhombic phase, reflecting the variation of the band gap between the three phases. The different splitting characteristics and the shifts along the energy axis must both be taken into account if the cubic or tetragonal phase are chosen as a substitute for the structurally more complicated orthorhombic phase, as has frequently been done in earlier theoretical studies of KNbO$_3$ in order to reduce the computational effort.

The nonlinear optical response of the orthorhombic phase was both measured with a tunable laser in the energy range between 1.2 and 1.6 eV and theoretically modeled in the independent-(quasi)particle approximation. We find a large impact not only of the underlying atomic geometry but also of the scissors shift on the calculated nonlinear susceptibility regarding the peak positions, peak forms, and overall magnitude of the coefficients. We also observe larger differences between the tetragonal and orthorhombic phase than in linear optics. Our results obtained with an appropriate scissors shift deduced from the evGW_0 approximation agree well with the novel experimental data reported in this work and are consistent with previous theoretical studies. The puzzling discrepancy between earlier DFT results and experimental data for some components, notably zzz, is thus no longer present. Instead, the inclusion of a scissors shift to account for quasiparticle effects in the electronic band structure leads to excellent agreement with the available experimental data for all components.

[1] D. Z. Shen, Prog. Cryst. Growth Charact. **20**, 161 (1990).

[2] C. Lu, S. Lo, and H. C. Lin, Mater. Lett. **34**, 172 (1998).

[3] Y. Saito, H. Takao, T. Tani, T. Nonoyama, K. Takatori, T. Homma, T. Nagaya, and M. Nakamura, Nature (London) **432**, 84 (2004).

[4] W. Lee, H. Han, A. Lotnyk, M. A. Schubert, S. Senz, M. Alexe, D. Hesse, S. Baik, and U. Gösele, Nat. Nanotechnol. **3**, 402 (2008).

[5] M. D. Fontana, G. Métrat, J. L. Servoin, and F. Gervais, J. Phys. C **17**, 483 (1984).

[6] S. Kim, J.-H. Lee, J. Lee, S.-W. Kim, M. H. Kim, S. Park, H. Chung, Y.-I. Kim, and W. Kim, J. Am. Chem. Soc. **135**, 6 (2013).

[7] E. Wiesendanger, Ferroelectrics **6**, 263 (1973).

[8] D. G. Bozinis and J. P. Hurrell, Phys. Rev. B **13**, 3109 (1976).

[9] J. P. Sokoloff, L. L. Chase, and D. Rytz, Phys. Rev. B **38**, 597 (1988).

[10] L. Holtmann, K. Buse, A. Groll, H. Hesse, and E. Krätzig, Appl. Phys. A **53**, 81 (1991).

[11] L. Grigorjeva, D. K. Millers, V. Pankratov, R. T. Williams. R. I. Eglitis, E. A. Kotomin, and G. Borstel, Solid State Commun. **129**, 691 (2004).

[12] C.-Z. Wang, R. Yu, and H. Krakauer, Phys. Rev. B **54**, 11161 (1996).

[13] E. E. Krasovskii, O. V. Krasovska, and W. Schattke, J. Electron. Spectrosc. Relat. Phenom. **83**, 121 (1997).

[14] C. M. I. Okoye, J. Phys.: Condens. Matter **15**, 5945 (2003).

[15] P. U. Sastry, Pramana J. Phys. **68**, 1001 (2007).

[16] Y.-Q. Xu, S.-Y. Wu, L.-N. Wu, and L.-J. Zhang, Mater. Sci. Semicond. Proc. **75**, 253 (2018).

[17] F. Schmidt, M. Landmann, E. Rauls, N. Argiolas, S. Sanna, W. G. Schmidt, and A. Schindlmayr, Adv. Mater. Sci. Eng. **2017**, 3981317 (2017).

[18] Y. Shiozaki, E. Nakamura, and T. Mitsui, Landolt-Börnstein, *New Series III/36A1* (2001).

[19] J. W. Liu, G. Chen, Z. H. Li, and Z. G. Zhang, Int. J. Hydrog. Energy **32**, 2269 (2007).

[20] T. Su, H. Jiang, H. Gong, and Y. Zhai, J. Mater. Sci. **45**, 3778 (2010).

[21] T. Zhang, K. Zhao, J. Yu, J. Jin, Y. Qi, H. Li, X. Hou, and G. Liu, Nanoscale **5**, 8375 (2013).

[22] T. Zhang, W. Lei, P. Liu, J. A. Rodriguez, J. Yu, Y. Qi, G. Liu, and M. Liu, Chem. Sci. **6**, 4118 (2015).

[23] P. G. Kang, B. K. Yun, S. Shin, J.-H. Ko, D.-J. Lee, Y.-S. Lee, and J. H. Jung, Mater. Sci. Eng. B **210**, 19 (2016).

[24] W. G. Schmidt, M. Albrecht, S. Wippermann, S. Blankenburg, E. Rauls, F. Fuchs, C. Rödl, J. Furthmüller, and A. Hermann, Phys. Rev. B **77**, 035106 (2008).

[25] A. Riefer, S. Sanna, A. Schindlmayr, and W. G. Schmidt, Phys. Rev. B **87**, 195208 (2013).

[26] L. Hedin, Phys. Rev. **139**, A796 (1965).

[27] A. Schindlmayr, in *Many-Electron Approaches in Physics, Chemistry and Mathematics* (Mathematical Physics Studies, Vol. 29), edited by V. Bach and L. Delle Site (Springer, Cham, 2014), pp. 343–357.

[28] C. Thierfelder, S. Sanna, A. Schindlmayr, and W. G. Schmidt, Phys. Status Solidi C **7**, 362 (2010).

[29] A. Riefer, M. Friedrich, S. Sanna, U. Gerstmann, A. Schindlmayr, and W. G. Schmidt, Phys. Rev. B **93**, 075205 (2016).

[30] Y. Uematsu, Jpn. J. Appl. Phys. **13**, 1362 (1974).

[31] I. Biaggio, P. Kerkoc, L.-S. Wu, P. Günter, and B. Zysset, J. Opt. Soc. Am. B **9**, 507 (1992).

[32] D. A. Roberts, IEEE J. Quantum Electron. **28**, 2057 (1992).

[33] J.-C. Baumert, J. Hoffnagle, and P. Günter, Proc. SPIE **0492**, 374 (1985).

[34] D. F. Xue and S. Y. Zhang, J. Phys. Chem. Solids **58**, 1399 (1997); Chem. Phys. Lett. **291**, 401 (1998).

[35] C.-G. Duan, W. N. Mei, J. Liu, and J. R. Hardy, J. Phys.: Condens. Matter **13**, 8189 (2001).

[36] S. Cabuk, Cent. Eur. J. Phys. **10**, 239 (2011).

[37] G. Kresse and J. Furthmüller, Comput. Mater. Sci. **6**, 15 (1996).

[38] P. E. Blöchl, Phys. Rev. B **50**, 17953 (1994).

[39] J. P. Perdew, A. Ruzsinszky, G. I. Csonka, O. A. Vydrov, G. E. Scuseria, L. A. Constantin, X. Zhou, and K. Burke, Phys. Rev. Lett. **100**, 136406 (2008); **102**, 039902(E) (2009).

[40] J. P. Perdew, K. Burke, and M. Ernzerhof, Phys. Rev. Lett. **77**, 3865 (1996); **78**, 1396(E) (1997).

[41] J. Sun, A. Ruzsinszky, and J. P. Perdew, Phys. Rev. Lett. **115**, 036402 (2015).

[42] Y. Zhang, J. Sun, J. P. Perdew, and X. Wu, Phys. Rev. B **96**, 035143 (2017).

[43] M. Shishkin and G. Kresse, Phys. Rev. B **74**, 035101 (2006).

[44] M. Shishkin and G. Kresse, Phys. Rev. B **75**, 235102 (2007).

[45] M. S. Hybertsen and S. G. Louie, Phys. Rev. B **34**, 5390 (1986).

[46] A. A. Mostofi, J. R. Yates, Y.-S. Lee, I. Souza, D. Vanderbilt, and N. Marzari, Comput. Phys. Commun. **178**, 685 (2008).

[47] S. Albrecht, L. Reining, R. Del Sole, and G. Onida, Phys. Rev. Lett. **80**, 4510 (1998).

[48] A. Chantzis, A. D. Laurent, C. Adamo, and D. Jacquemin, J. Chem. Theory Comput. **9**, 4517 (2013).

[49] S. Hirata and M. Head-Gordon, Chem. Phys. Lett. **314**, 291 (1999).

[50] T. Sander, E. Maggio, and G. Kresse, Phys. Rev. B **92**, 045209 (2015).

[51] W. G. Schmidt, S. Glutsch, P. H. Hahn, and F. Bechstedt, Phys. Rev. B **67**, 085307 (2003).

[52] B. Adolph, V. I. Gavrilenko, K. Tenelsen, F. Bechstedt, and R. Del Sole, Phys. Rev. B **53**, 9797 (1996).

[53] R. Leitsmann, W. G. Schmidt, P. H. Hahn, and F. Bechstedt, Phys. Rev. B **71**, 195209 (2005).

[54] B. F. Levine and C. G. Bethea, Appl. Phys. Lett. **20**, 272 (1972).

[55] R. C. Miller, Appl. Phys. Lett. **5**, 17 (1964).

[56] I. H. Malitson, J. Opt. Soc. Am. **55**, 1205 (1965).

[57] G. Shirane, R. Newnham, and R. Pepinsky, Phys. Rev. **96**, 581 (1954).

[58] A. W. Hewat, J. Phys. C **6**, 2559 (1973).

[59] L. Katz and H. D. Megaw, Acta Crystallogr. **22**, 639 (1967).

[60] S. Cabuk, Optoelectron. Adv. Mater. Rapid Commun. **1**, 100 (2007), and references therein.

[61] M. Friedrich, A. Riefer, S. Sanna, W. G. Schmidt, and A. Schindlmayr, J. Phys.: Condens. Matter **27**, 385402 (2015).

[62] E. K. Chang, E. L. Shirley, and Z. H. Levine, Phys. Rev. B **65**, 035205 (2001).

[63] E. Luppi, H. Hübener, and V. Véniard, Phys. Rev. B **82**, 235201 (2010).

[64] A. Riefer and W. G. Schmidt, Phys. Rev. B **96**, 235206 (2017).